Mon. Not. R. Astron. Soc. **399,** 750–761 (2009) doi:10.1111/j.1365-2966.2009.15301.x

Studying X-ray reprocessing and continuum variability in quasars: PG 1211+143

R. Bachev,[1⋆] D. Grupe,[2⋆] S. Boeva,[1] E. Ovcharov,[3] A. Valcheva,[1,3] E. Semkov,[1] Ts. Georgiev[1] and L. C. Gallo[4⋆]

[1]*Institute of Astronomy, Bulgarian Academy of Sciences, Sofia 1784, Bulgaria*
[2]*Department of Astronomy and Astrophysics, Pennsylvania State University, 525 Davey Lab, University Park, PA 16802, USA*
[3]*Department of Astronomy, Sofia University, 5 James Bourchier Street, 1164 Sofia, Bulgaria*
[4]*Department of Astronomy and Physics, Saint Mary's University, Halifax, NS B3H 3C3, Canada*

Accepted 2009 June 24. Received 2009 June 1; in original form 2009 January 16

ABSTRACT

We present the results from a monitoring campaign of the Narrow-Line Seyfert 1 galaxy PG 1211+143. The object was monitored with ground-based facilities (*UBVRI* photometry; from 2007 February to July) and with *Swift* [X-ray photometry/spectroscopy and ultraviolet (UV)/optical photometry; between 2007 March and May]. We found PG 1211+143 in a historical low X-ray flux state at the beginning of the *Swift* monitoring campaign in 2007 March. It is seen from the light curves that while violently variable in X-rays, the quasar shows little variations in optical/UV bands. The X-ray spectrum in the low state is similar to other narrow-line Seyfert 1 galaxies during their low states and can be explained by a strong partial covering absorber or by X-ray reflection on to the disc. With the current data set, however, it is not possible to distinguish between both scenarios. The interband cross-correlation functions indicate a possible reprocessing of the X-rays into the longer wavelengths, consistent with the idea of a thin accretion disc, powering the quasar. The time lags between the X-ray and the optical/UV light curves, ranging from ∼2 to ∼18 d for the different wavebands, scale approximately as $\sim\lambda^{4/3}$, but appear to be somewhat larger than expected for this object, taking into account its accretion disc parameters. Possible implications for the location of the X-ray irradiating source are discussed.

Key words: accretion, accretion discs – galaxies: active – galaxies: photometry – quasars: general – quasars: individual: PG 1211+143.

1 INTRODUCTION

Powered by accretion, supposedly on to a supermassive black hole, quasars [active galactic nuclei (AGN)] are long known mostly as highly energetic, exotic objects in the hearts of the galaxies. Not until recently was their key role in galaxy evolution realized, revealed mostly as a strong correlation between the properties of the central black hole and that of the host galaxy (Magorrian et al. 1998; Ferrarese & Merritt 2000). Studying quasars, therefore, is not only important to understand the underlying physics; it can also help to shed some light on the strange interplay between the accreting matter from the host and outflows from the centre, which ultimately shape both the black hole and the galaxy.

⋆E-mail: bachevr@astro.bas.bg (RB); grupe@astro.psu.edu (DG); lgallo@ap.stmarys.ca (LCG)

Although a general picture of the structure of a typical quasar seems to be widely accepted (e.g. Elvis 2000; see also Krolik 1999), there are still many details in this picture that are not fully understood. Many of the problems to be solved concern AGN continuum variability – a rather common property, observed in practically all energy bands. Its universality indicates perhaps that variability should be an intrinsic property of the processes, responsible for continuum generation. The optical/ultraviolet (UV) to X-ray part of the continuum spectrum, as typically assumed, originates from an accretion disc around the central supermassive black hole.

Generally, X-ray variability can be caused by several factors: a change in the accretion rate; variable absorption (e.g. Abrassart & Czerny 2000); variable reflection (e.g. through a change of the height of the irradiating source; Miniutti & Fabian 2004; see also Gallo 2006; Done & Nayakshin 2007); some combination of reflection and absorption (e.g. Chevalier et al. 2006; Turner & Miller 2009); hotspots orbiting the central black hole (Turner et al. 2006; Turner & Miller 2009); local flares (Czerny et al. 2004), etc.

© 2009 The Authors. Journal compilation © 2009 RAS

The AGN type with the strongest X-ray variability is the class of narrow-line Seyfert 1 galaxies (NLS1s; e.g. Osterbrock & Pogge 1985). In addition, NLS1s show the steepest X-ray spectra seen among all AGN (e.g. Boller, Brandt & Fink 1996; Brandt, Mathus & Elvis 1997; Leighly 1999a,b; Grupe, Thomas & Beuermann 2001). Most of their observed properties, like spectral slopes, Fe II and [O III] line ratios, C IV shifts, etc., appear to be driven by the relatively high Eddington ratio $L/L_{\rm Edd}$ in these objects (e.g. Sulentic et al. 2000; Boroson 2002; Bachev et al. 2004; Grupe 2004).

What concerns the optical/UV variability, the picture there is even more puzzling. There are many factors that can contribute to the variations of the optical flux, but most of them can account for the long-term (months to years) changes. There are often reported in many objects, however, short-term (day to week) optical/UV variations, simultaneous with or shortly lagging behind the X-ray variations. An interesting idea that can explain such a behaviour is reprocessing of the highly variable X-ray emission into optical/UV bands.

In this paper, we address the question of the relations between the X-ray and the optical/UV emission by studying the variability from X-rays to *I* band of the NLS1 PG 1211+143. This NLS1 has been the target of almost all major X-ray observatories since *Einstein* (Elvis, Wilkes & Tananbaum 1985). The X-ray continuum displays a strong and variable soft X-ray excess (Pounds & Reeves 2007). From *XMM–Newton* Reflection Grating Spectrometer data, Pounds et al. (2003) suggested the presence of high-velocity outflows in PG 1211+143, a result that was questioned by Kaspi & Behar (2006). However, high-velocity outflows seen in X-rays have been repeatedly reported (e.g. Leighly et al. 1997) and new *XMM–Newton* data of PG 1211+143 (Pounds & Page 2006) seem to confirm the previous claims made by Pounds et al. (2003).

Our primary goal is to find out if and how the X-ray variations are transferred into the longer wavelength continuum. Time delays between the flaring X-ray emission, presumably coming from a compact, central source and the optical/UV light curves (LCs) are expected, provided the X-rays are reprocessed in the outer, colder part of an accretion disc. Such a study may have implications on two important problems – the radial temperature distribution of an accretion disc (and hence the type of the disc) and the location of the X-ray source, based on how much the disc 'sees' it.

This paper is organized as follows. In Section 2, we describe the *Swift* and ground-based optical monitoring observations. Section 3 focuses on presenting the results of this study and in Section 4 we discuss these results in the context of the general picture of AGN. Throughout the paper, spectral indexes are denoted as energy spectral indexes with $F_\nu \propto \nu^{-\alpha}$. Luminosities are calculated assuming a Λ cold dark matter cosmology with $\Omega_{\rm M} = 0.27$, $\Omega_\Lambda = 0.73$ and a Hubble constant of $H_0 = 75$ km s^{-1} Mpc^{-1}.

2 OBSERVATIONS AND REDUCTIONS

2.1 *Swift* data

The *Swift* gamma-ray burst (GRB) explorer mission (Gehrels et al. 2004) monitored PG 1211+143 between 2007 March 08 and May 20. Note that scheduled observations were twice bumped by detections of GRBs,[1] explaining the absence of segments 15 and 20 (Table A1). After our monitoring campaign in 2007, PG 1211+143 was re-observed by *Swift* in 2008 February (segment 24). However, this observation was used to slew between two targets. Therefore, this observation is very short (188 s) and no X-ray spectra or UV/Optical Telescope (UVOT) photometry data were obtained. This observation only allows to measure a count rate. A summary of all *Swift* observations is given in Table A1. The *Swift* X-ray telescope (XRT; Burrows et al. 2005) was operating in photon counting mode (Hill et al. 2004) and the data were reduced by the task XRTPIPELINE version 0.10.4, which is included in the HEASOFT package 6.1. Source photons were selected in a circular region with a radius of 47 arcsec and background region of a close by source-free region with $r = 188$ arcsec. Photons were selected with grades 0–12. The photons were extracted with XSELECT version 2.4. The spectral data were rebinned by using GRPPHA version 3.0.0 having 20 photons per bin. The spectra were analysed with XSPEC version 12.3.1 (Arnaud 1996). The ancillary response function files (arfs) were created by XRTMKARF and corrected for vignetting and bad columns/pixels using the exposure maps. We used the standard response matrix *swxpc0to12s0_20010101v010.rmf*. Especially during the low state, the number of photons during one segment is too small to derive a spectrum with a decent signal-to-noise ratio. Therefore, we co-added the data of several segments to obtain source and background spectra. In order to examine spectral changes at different flux/count rate levels, we created spectral for the low, intermediate and high states with count rates CR < 0.12 counts s^{-1}, $0.13 <$ CR < 0.2 and CR > 0.2 counts s^{-1}. This lead to high-state source and background spectra co-adding the data from 2007 April 22, May 09 and 14 (segments 018, 021 and 022), 2007 March 26 and April 02 (segments 13 and 14) for the intermediate state, and all other for the low state. As for the arfs, we created an arf for each segment and co-added them by using the ftool ADDARF weighted by the exposure times. Due to the low number of photons in the 2008 February observation (segment 024) no spectra could be derived. Fluxes in the 0.2–2.0 and 2–10 keV band for this segment were determined from the count rates in these bands by comparing the fluxes during the high state during segments 018, 021 and 022, assuming no spectral changes. All spectral fits were performed in the observed 0.3–10.0 keV energy band. In order to compare the observations from different missions, we use the HEASARC tool PIMMS version 3.8.

Data were also taken with the UVOT (Roming et al. 2005), which operates between 1700 and 6500 Å using six photometry filters. Before analysing the data, the exposures of each segment were co-added by the UVOT task UVOTIMSUM. Source counts were selected with the standard 5 arcsec radius in all filters (Poole et al. 2008) and background counts in a source-free region with a radius $r = 20$ arcsec. The data were analysed with the UVOT software tool UVOTSOURCE assuming a GRB-like power-law continuum spectrum. The magnitudes were all corrected for Galactic reddening $E_{B-V} = 0.035$ given by Schlegel, Finkbeiner & Davis (1998) using the extinction correction in the UVOT bands given in Roming et al. (2009).

2.2 *XMM–Newton* data analysis

In order to compare the results derived from the *Swift* observations, we also analysed the *XMM–Newton* data of PG 1211+143. *XMM–Newton* observed PG 1211+143 on 2001 June 15 and 2004 June 21 for 53 and 57 ks, respectively (Pounds & Reeves 2007). Because our paper focuses on the *Swift* and ground-based monitoring campaigns in 2007, we reduced only the *XMM–Newton* EPIC pn

[1] Although *Swift* has turned into a multipurpose observatory, its main focus is still on observing GRBs and therefore GRBs will supersede scheduled Target of Opportunity observations.

data. A complete analysis of these *XMM–Newton* data sets can be found in Pounds et al. (2003), Pounds & Page (2006) and Pounds & Reeves (2007). The *XMM–Newton* EPIC pn data were reduced in the standard way as described, for example, in Grupe, Mathur & Komossa (2004).

2.3 Ground-based observations

Additional broad-band monitoring in *UBVRI* bands was performed on three telescopes: the 2-m RCC and the 50/70-cm Schmidt telescopes of Rozhen National Observatory, Bulgaria and the 60-cm telescope of Belogradchik Observatory, Bulgaria. All telescopes are equipped with CCD cameras: the 2-m telescope with a VersArray CCD, while the smaller telescopes with SBIG ST-8. Identical $(U)BVR_cI_c$ filters are used in all telescopes. The ground-based monitoring covered a period of about 5 months (2007 February–July), during which the object was observed in more than 40 epochs in *BVRI* bands, and occasionally in *U*. The photometric errors varied significantly depending on the telescope, the filter, the camera in use and the atmospheric conditions, but were typically 0.02–0.03 mag (rarely up to ∼0.1 mag in some filters for the smaller instruments).

3 RESULTS

3.1 Long-term X-ray light curve

Fig. 1 displays the long-term 0.2–2.0 and 2.0–10.0 keV LCs. Most of the data prior 2000 were taken from Janiuk, Czerny & Madejski (2001). The *ROSAT* All-Sky Survey point at 1990.9 was taken from Grupe et al. (2001). The *XMM* 2001 and 2004 and the *Swift* fluxes were from our analysis as presented in this paper. PG 1211+143 has become fainter over the last decades in both soft and hard bands with the strongest changes in the soft band. Historically, in the early 1980s, PG 1211+143 had been in a much brighter X-ray state than over the last decade. During the beginning of the *Swift* monitoring campaign in 2007 March, PG 1211+143 appeared to be in the lowest state seen so far. At the end of our monitoring campaign in 2007 May, PG 1211+143 was back in the high state that was previously known from the *XMM* observations. The latest data point

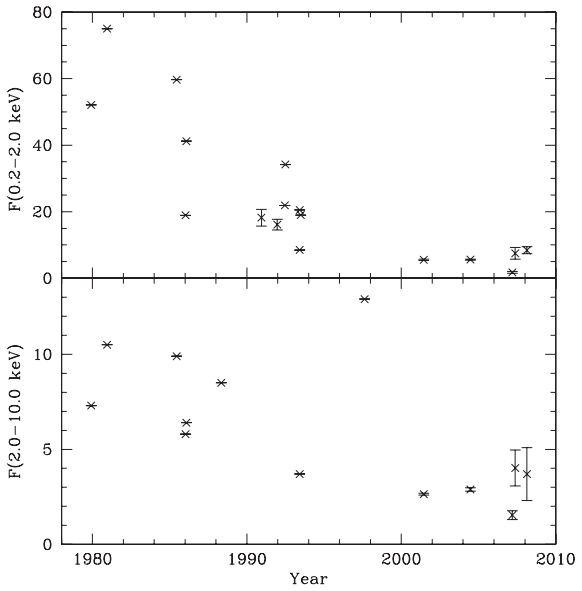

Figure 1. Long-term 0.2–2.0 and 2.0–10.0 keV X-ray LCs of PG 1211+143. The fluxes are given in units of 10^{-12} erg s^{-1} cm $^{-2}$.

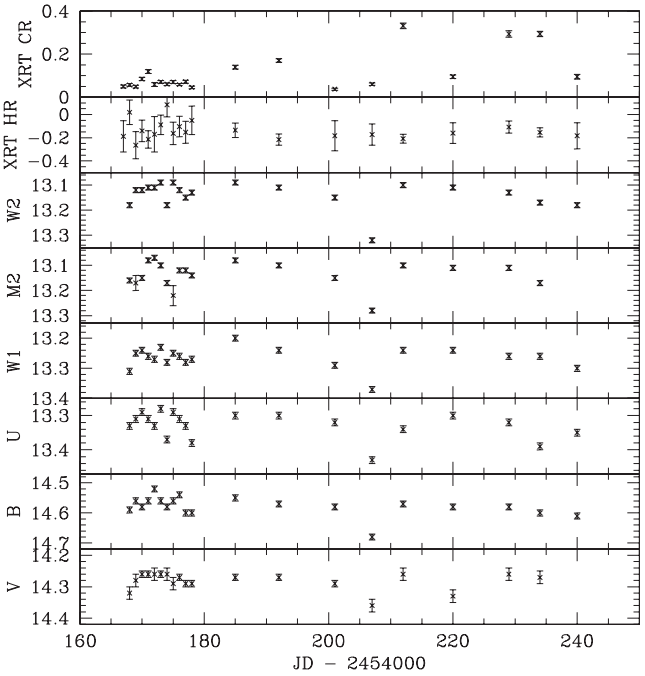

Figure 2. *Swift* XRT and UVOT LCs. The XRT count rates are given in units of counts s^{-1}. The hardness ratio is defined in Section 3.2. All UVOT magnitudes are corrected for Galactic reddening ($E_{B-V} = 0.035$; Schlegel et al. 1998).

is from 2008 February. The 0.2–2.0 and 2–10 keV fluxes during that observation are comparable with the *XMM* observations. As for the *Swift* data taken in 2007 and 2008, we used the flux values obtained from the low- and high-state spectra. As for the 2008 February data flux points, we converted the count rates into fluxes assuming an X-ray spectrum as seen during the *Swift* high states.

3.2 *Swift* XRT and UVOT light curves

The *Swift* XRT count rates and hardness ratios,[2] and UVOT magnitudes are listed in Table A2. These values are plotted in Fig. 2. At the beginning of the *Swift* monitoring campaign in 2007 March, PG 1211+143 was found in a very low state. Compared to previous *ROSAT* and *XMM–Newton* observations, reported by, for example, Grupe et al. (2001) and Pounds et al. (2003), PG 1211+143 appeared to be fainter by a factor of about 10. At the end of the monitoring campaign in 2007 May, PG 1211+143 reached a flux level that was expected from the previous *ROSAT* and *XMM–Newton* observations. A later observation by *Swift* on 2008 February 17 found it at a level of 0.375 ± 0.045 counts s^{-1} and confirmed that it returned back in a high state. The low state, found in 2007 March, seems to be just a short temporary event. A behaviour like this is not unseen in AGN and has been recently reported for the NLS1 Mkn 335 by Grupe, Komossa & Gallo (2007b) and Grupe et al. (2008a), which had been found in a historical low state by *Swift* and *XMM–Newton*.

Besides the X-ray variability, PG 1211+143 also displays some variability at optical/UV wavelengths, although on a much smaller level than in X-rays. Table A2 lists the magnitudes measured in all six UVOT filters. All six LCs are also plotted in Fig. 2. The

[2] The XRT hardness ratio is defines as HR = $(H - S)/(H + S)$ with S and H are the counts in the 0.3–1.0 keV and 1.0–10.0 keV bands, respectively.

most significant drop occurred in all six filters during the 2007 April 17 observation. During the next observation on 2007 April 22, PG 1211+143 not only became brighter again in the optical/UV but also showed an increase in count rate by a factor of almost 4 in X-rays.

3.3 Ground-based monitoring

3.3.1 Secondary standards

In order to facilitate future photometric studies of PG 1211+143, we calibrated secondary standards in the field of the object, shown as stars 'A' (USNO B1 1039-0200330) and 'B' (USNO B1 1040-0199800) in Fig. 3. The magnitudes with the errors (due primarily to the errors of the calibration) are given in Table 1. Mostly Landolt standard sequences (Landolt 1992) were used for the calibration (PG 1633+099) and in some occasions M67 (Chevalier & Ilovaisky 1991).

3.3.2 Magnitude adjustments

The LC of PG 1211+143 (Section 3.4) is built by measuring its differential magnitude with respect to the adjacent field stars, none of which showed signs of variability (with the exception of a known RR Lyr type star, CI Com, located very close to the quasar). Since the data are collected on different instruments using different cameras (even with identical filters), it is not unusual for an object with strong emission lines to show a differential magnitude, slightly depending on the instrument. The reason for this complication is mostly related to the nature of the quasar spectrum: if a strong emission line falls in a wavelength region where the cameras have different sensitivities, or the filter transparency is slightly different, one may get a broad-band differential magnitude depending on the instrument. In our case, all *R*-band magnitudes of the quasar had to be adjusted by 0.1 mag for one of the instruments (the 50/70 cm Schmidt telescope), probably due to the reasons described above. The adjustment corrections were easily obtained through comparison of the LCs, which cover each other on many occasions. We should note, however, that the exact quasar magnitudes are not of importance for this study, as the variations are only considered.

Additionally, the ground-based *UBV* magnitudes were similarly adjusted to match the corresponding *Swift* magnitudes. Actually, after the correction for the Galactic reddening, the adjustments for the ground-based *B* and *V* magnitudes were very minor, typically less than 0.03 mag, which is smaller than the uncertainties of the calibrated field standards (Section 3.3.1).

A log of the ground-based observations, including the obtained *UBVRI* magnitudes of the quasar after the corrections for the Galactic reddening, is presented in Table A3.

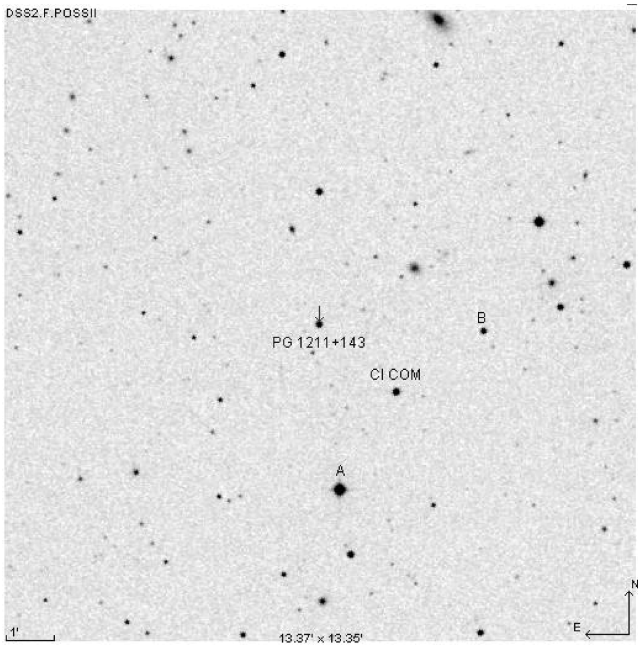

Figure 3. Stars in the filed of PG 1211+143, used for the ground-based differential photometry. Their optical (*BVRI*) magnitudes are calibrated and shown in Table 1. A nearby RR Lyr variable is also shown. CDS Aladin service was used to generate the picture.

Table 1. Field standards.

Star	*B*	*V*	*R*	*I*
A	11.80 (0.08)	11.35 (0.05)	10.97 (0.06)	10.71 (0.05)
B	–	15.34 (0.10)	14.80 (0.07)	14.35 (0.07)

3.4 Combined light curves

The combined continuum LCs of PG 1211+143 for the time of monitoring are presented in Figs 4 and 5. Fig. 4 compares the X-ray with the optical (*UBVRI*) variations, all transformed into arbitrary magnitudes for presentation purposes. The optical data are combined from all participating instruments. One sees that the erratic X-ray variations (almost 2.5 mag) hardly influence the optical flux, which shows only minor variations on a generally decaying trend. Fig. 5 presents the most intense period of the monitoring, comparing X-ray and *V*-band magnitudes. The *V*-band LC for that period stays remarkably stable, with a rms smaller or comparable to the typical photometric errors.

3.5 Time delays

In order to study the time delay dependence of the wavelength, we performed a linear-interpolation cross-correlation analysis (Gaskell & Sparke 1986) between the X-ray and the other bands LCs. The interpolation between the photometric points is needed due to unevenly sampled data and is one of the frequently used methods. Other methods applied in the literature do not seem to obtain significantly different results (e.g. discrete cross-correlation function (CCF), Edelson & Krolik 1988; *z*-transformed CCF, Alexander 1997) when compared.

Fig. 6 shows the interpolation cross-correlation functions, ICCF(τ), between the X-ray LC and the other band LCs. A maximum of an ICCF(τ) for a positive τ indicates a time delay behind the X-ray changes and is a signature of a possible reprocessing. Although the ICCFs are mostly negative, due to the different overall trends of the X-ray and optical/UV wavebands, a clear maximum for a positive τ is evident for most wavebands.

Since the X-ray points distribution was far from a Gaussian, even on a magnitude scale, a rank correlation was attempted, but the resulting ICCFs appeared to be very similar.

Table 2 and Fig. 7 show the wavelength dependence of the time lag. The wavelengths are taken from the corresponding transmission

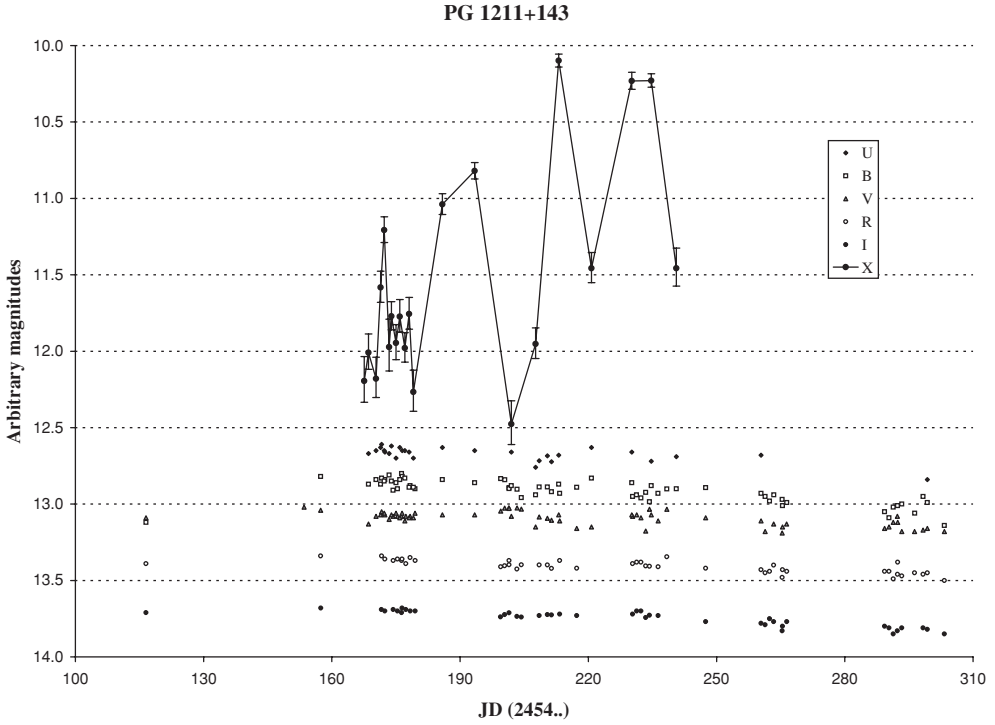

Figure 4. Optical (*UBVRI*) and X-ray LCs for the time of the monitoring (2007 February–July). Where necessary, arbitrary constants are added to the magnitudes to separate the curves and improve the presentation (see the text). The X-ray count rates are converted into arbitrary magnitudes [using $m_X = -2.5 \log(\mathrm{CR}) + \mathrm{constant}$] for a better comparison with the optical variability. The optical data are combined from all instruments.

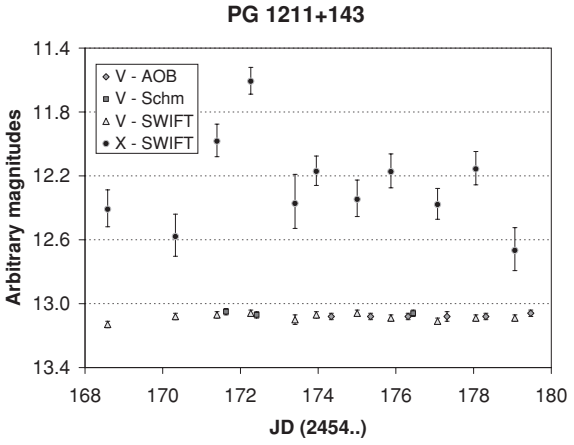

Figure 5. The most intensive 12 days of the monitoring, where the quasar was observed typically twice a day in the optical. The *V*-band LC (magnitudes from the participating ground-based observatories: Rozhen Schmidt camera and Belogradchik reflector, and *Swift* UVOT are shown separately) and the X-ray LC (in arbitrary magnitudes) are compared in the figure. One sees the significant X-rays variations and almost constant optical flux (the standard deviation of the *V*-band magnitudes for this period is smaller than the average photometric error).

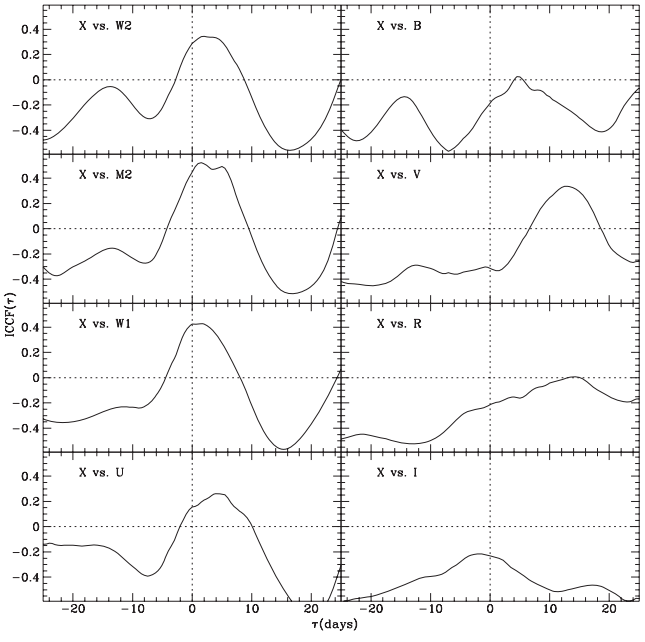

Figure 6. The interpolated cross-correlation functions between the X-ray LC and the optical/UV LCs. A clear peak for a positive τ, indicating an optical/UV delay behind the X-rays is visible in most cases. The ICCFs are mostly negative due to the different overall trends of the X-ray and the optical emission (see the text).

curve of the filters used (with uncertainties associated with the bandwidths) and the time delays are from the ICCF maxima.

One sees that for the *I* band the highest peak of the ICCF (Fig. 6) is at $\tau \simeq -2$d, indicating a possible short lag of the X-rays behind the near-infrared emission. Another, lower peak at $\tau \simeq +18$ d is also evident. This maximum could probably be associated with reprocessing and is plotted in Fig. 7 mostly to demonstrate its consistency with the fit (see below). However, the *I*-band response to the X-ray variations seems to be more complicated than the simple reprocessing model suggests, as we discuss later in Section 4.

Uncertainties of the maximum of the ICCFs are difficult to assess. Although there are methods, described in the literature (Gaskell &

Table 2. Wavelength dependence of the time delays with uncertainties. For *I*-band, the highest and the first positive (in parentheses) ICCF maxima are shown (see the text).

Filter	λ_0 (Å)	FWHM (Å)	τ (d)	$\Delta\tau$ (d)
UVW2	1928	657	2.5	3
UVM2	2246	498	2.5	3.5
UVW1	2600	693	2	3
U	3465	785	4	3.5
B	4392	975	5	3.5
V	5468	769	13	3
R	∼6500	∼700	14	4
I	∼8300	∼1000	−2 (18)	3 (4)

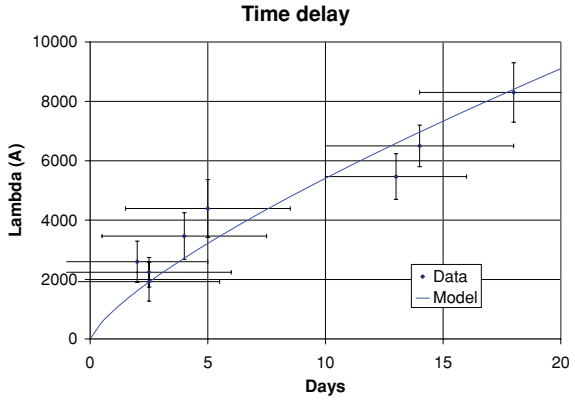

Figure 7. Time lags versus the wavelength. The wavelength uncertainties are due to the filter transmission curves and the time ones due to the ICCF peak widths (see the text). Data points correspond to *UVW2*, *UVM2*, *UVW1*, *U*, *B*, *V*, *R* and *I* filters, from bottom to top, respectively. For *I*-band, the first positive maximum is plotted; however, a stronger maximum at $\tau \simeq -2$d is evident from Fig. 6, possibly indicating that the reprocessing perhaps also plays a role, but is not the main factor, leading to a casual connection between the LCs. A fit to the data [$\tau_\lambda \simeq 9\lambda_{5000}^{4/3}$ (d)] is also shown, indicating that the delay scales as expected for a standard accretion disc. The data, however, are not stringent enough to rule out other possibilities, since different fits are also possible.

Peterson 1987), one can hardly rely completely on so computed uncertainties, since the true behaviour of the LC at the places where it is interpolated is anyway impossible to predict. That is why we accepted the width of ICCF profile at an appropriate level around the peak as an indicative of the uncertainty. This approach is very simple and in addition incorporates into the errors such unknowns as the inclination of the disc with respect to the observer, the spatial size of the irradiating source, etc. See Bachev (2009) for more discussions on these issues.

A clear relation between τ and λ is seen and an acceptable (non-linear) fit to the data is $\tau_\lambda \simeq 9\lambda_{5000}^{4/3}$ (d),[3] where λ_{5000} is $\lambda/5000$Å. Section 4 discusses possible implications of this result and how it fits into the model of reprocessing from a thin accretion disc.

[3] All the calculations here are performed using the observer's frame measurements. Due to the similar way, the times and the wavelengths are affected by the redshift, for the quasar rest frame the delay in the $\tau - \lambda$ dependence *increases* only by $(1+z)^{-1/3}$, Section 4, which is only ∼3 per cent and is much less than the expected errors.

3.6 X-ray spectroscopy

As described in Section 2.1, the data were combined to derive low, intermediate and high-state spectra of PG 1211+143. These data were first fitted by a single absorbed power-law model with the absorption column density fixed to the Galactic value (2.47×10^{20} cm^{-2}; Kalberla et al. 2005). Table 3 lists the spectral fit parameters. Obviously a single power-law model does not represent the observed spectrum. Fig. 8 displays this fit simultaneously to the low- and high-state *Swift* spectra. As a comparison, Table 3 also lists the results for the fits to the 2001 and 2004 *XMM–Newton* EPIC pn data. As the next step, we fitted the spectra with a broken power-law model. Although this model significantly improves the fits and describes the spectra quite well, it is not a physical model. Especially in the low state the hard X-ray spectral slope appears to be very flat with $\alpha_X = -0.18$. This behaviour is typical when the X-ray spectrum is affected by either partial covering absorption or reflection (e.g. Turner & Miller 2009; Grupe et al. 2008a).

Next, the spectra were fitted with a power-law model with a partial covering absorber. These fits suggest a strong partial covering absorber in the low-state spectrum with an absorption column density of the order of 9×10^{22} cm^{-2} and a covering fraction of 95 per cent. During the intermediate state, the column density of the absorber decreases to 8×10^{22} cm^{-2} with a covering fraction of 93 per cent and drops down to $N_{\rm H,pc} = 3.5 \times 10^{22}$ cm^{-2} and $f_{\rm pc} =$ 78 per cent during the high state. In order to check whether the data can be self-consistently fit, we fitted the low- and high-state *Swift* data simultaneously in XSPEC. In this case, we tied the column densities of the partial covering absorber and the X-ray spectral slopes of both spectra but left the covering fractions and the normalizations free. Here, we found an absorption column density of $N_{\rm H,pc} = 8.1 \times 10^{22}$ cm^{-2} with covering fractions of 91 and 86 per cent for the low and high states, respectively. In all cases, *Swift* as well as *XMM–Newton*, the X-ray spectral slope remains around $\alpha_X = 2.1$ and does not show any significant changes within the errors. The partial covering absorber model can explain the variability seen in X-rays in PG 1211+143. The results obtained from the *Swift* data during the high state are consistent with those derived from the 2001 and 2004 *XMM–Newton* EPIC pn data.

The spectra were also fitted with a blurred reflection model (Ross & Fabian 2005). Such models, where the primary emission (i.e. the power-law component) illuminates the accretion disc producing a reflection spectrum that is blurred by Doppler and relativistic effects close to the black hole (e.g. Fabian et al. 1989), have been successfully applied to several NLS1 X-ray spectra (e.g. Fabian et al. 2004; Gallo et al. 2007a,b; Grupe et al. 2008a; Larsson et al. 2008). As shown in Figs 9 and 10, the reflection model broadly describes the high- and low-flux states of PG 1211+143. In the simplest case, the blurring parameters and disc ionization are linked between the two epochs. The disc inclination (i) and outer radius ($R_{\rm out}$) are fixed to 30° and $400R_{\rm g}$, respectively; $R_{\rm g}$ is the Schwarzschild radius. The continuum shape (Γ) and normalizations of the reflection and power law were free to vary independently at each epoch. The resulting fit is reasonable (χ^2_ν/degree of freedom = 1.30/105), considering the obvious oversimplification of our model. The inner disc radius and emissivity index were found to be $R_{\rm in} = 1.76^{+0.27}_{-0.35} R_{\rm g}$ and $q = 5.57^{+0.54}_{-0.71}$, respectively. The disc ionization was $\xi = 116 \pm 10$. The intrinsic power-law shape was significantly harder during the low-flux state, $\alpha_{\rm X,low} = 0.55^{+0.09}_{-0.06}$, compared to $\alpha_{\rm X,high} = 0.96^{+0.13}_{-0.10}$ during the high state. The primary difference between the high and low state is the relative contribution of the power-law component to the total

Table 3. Spectral analysis of the X-ray low and high states of PG 1211+143 with the Galactic absorption column density set to 2.47×10^{20} cm^{-2} given by Kalberla et al. (2005).

Model	$\alpha_{\rm X,soft}$	$E_{\rm Break}$	$\alpha_{\rm X,hard}$	$N_{\rm H,pc}$	$f_{\rm pc}$	χ^2/ν	$F_{0.2-2.0\,\rm keV}$	$F_{2-10\,\rm keV}$
				Low state				
Powl	1.73 ± 0.10	–	–	–	–	312/60	1.59 ± 0.10	0.39 ± 0.02
Bknpo	$2.29^{+0.14}_{-0.13}$	$1.42^{+0.13}_{-0.11}$	$-0.18^{+0.17}_{-0.18}$	–	–	68/58	1.81 ± 0.16	2.45 ± 0.21
Zpcfabs * powl	$2.18^{+0.10}_{-0.12}$	–	–	$9.45^{+1.87}_{-1.62}$	0.95 ± 0.02	82/58	1.76 ± 0.26	1.54 ± 0.23
				Intermediate state				
Powl	1.71 ± 0.15	–	–	–	–	103/26	3.65 ± 0.36	0.92 ± 0.09
Bknpo	2.44 ± 0.26	$1.15^{+0.27}_{-0.14}$	$0.31^{+0.26}_{-0.34}$	–	–	30/24	4.34 ± 0.76	3.85 ± 0.67
Zpcfabs * powl	2.22 ± 0.20	–	–	$7.88^{+3.21}_{-2.33}$	$0.93^{+0.03}_{-0.04}$	35/24	4.07 ± 1.47	2.84 ± 1.04
				High state				
Powl	1.47 ± 0.06	–	–	–	–	168/62	7.04 ± 0.29	2.76 ± 0.12
Bknpo	$2.05^{+0.16}_{-0.15}$	$1.04^{+0.13}_{-0.12}$	0.84 ± 0.14	–	–	91/60	7.79 ± 0.78	5.06 ± 0.51
Zpcfabs * powl	1.98 ± 0.14	–	–	$3.48^{+1.99}_{-1.02}$	$0.78^{+0.05}_{-0.07}$	101/60	7.50 ± 1.76	4.02 ± 0.94
>				High- and Low-state simultaneously				
Powl	1.56 ± 0.05	–	–	–	–	488/123	1.49/7.24	0.50/2.41
Bknpo	2.14 ± 0.10	1.30 ± 0.12	$0.34^{+0.12}_{-0.12}$	–	–	215/121	1.79/7.65	1.62/6.92
Zpcfabs * Powl	2.00 ± 0.09	–	–	$8.11^{+1.64}_{-1.33}$	$0.91 \pm 0.02/0.86 \pm 0.03$	209/120	1.65/7.68	1.53/4.52
				XMM–Newton 2001				
Powl	1.97 ± 0.02	–	–	–	–	13092/994	5.56 ± 0.03	0.86 ± 0.01
Bknpo	2.20 ± 0.01	1.28 ± 0.05	0.71 ± 0.05	–	–	4860/992	5.57 ± 0.02	3.04 ± 0.02
Zpcfabs * powl	2.15 ± 0.01	–	–	6.41 ± 0.15	0.87 ± 0.02	5424/992	5.50 ± 0.10	2.64 ± 0.05
				XMM–Newton 2004				
Powl	1.62 ± 0.01	–	–	–	–	4122/940	5.63 ± 0.05	1.06 ± 0.02
Bknpo	1.75 ± 0.01	1.58 ± 0.05	0.85 ± 0.03	–	–	1828/938	5.58 ± 0.05	3.12 ± 0.03
Zpcfabs * powl	1.73 ± 0.01	–	–	8.73 ± 0.34	0.70 ± 0.02	1958/938	5.58 ± 0.17	2.89 ± 0.09

Note. The absorption column density of the partial covering absorber $N_{\rm H,pc}$ is given in units of 10^{22} cm^{-2} . $f_{\rm pc}$ denotes the covering fraction of the partial covering absorber. The observed 0.2–2.0 and 2–10 keV fluxes $F_{0.2-2.0\rm keV}$ and $F_{2-10\rm keV}$ are given in units of 10^{-12} erg s^{-1} cm^{-2}.

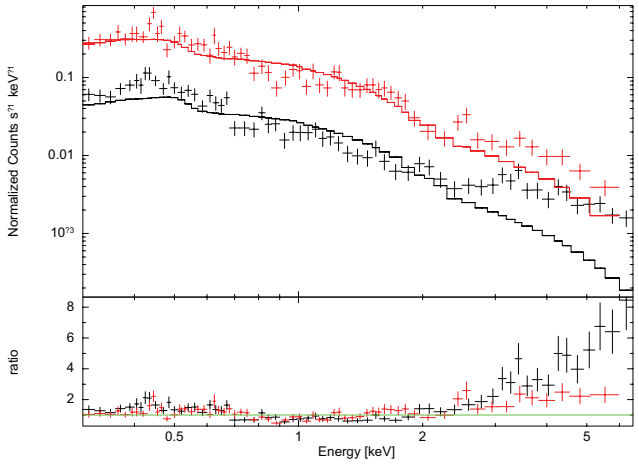

Figure 8. *Swift* XRT low- and high-state spectra fitted by an absorbed single power-law model. The black spectrum is the low and the red the high-state spectrum.

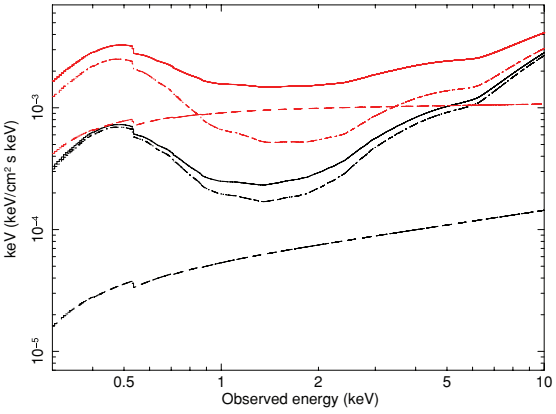

Figure 9. Blurred reflection model applied to the low- and high-state XRT spectra of PG 1211+143 with the black and red (the upper three) lines showing the models for the low- and high-state data, respectively.

0.3–10 keV flux, being approximately 0.42 and 0.12, respectively. During the low-flux state, the reflection component dominates the spectrum.

3.7 Spectral energy distribution

Fig. 11 displays the spectral energy distributions (SED) during the low-state observation on 2007 April 17 (blue squares) and the high-state observation on April 22 (red triangles). The optical/UV slope $\alpha_{\rm UV}$ slightly changes from -0.67 ± 0.12 to -0.56 ± 0.10 between the low and high states. Most significant, however, is the change in the optical-to-X-ray spectral slope $\alpha_{\rm ox}$[4] from $\alpha_{\rm ox} = 1.84$ during the low state to $\alpha_{\rm ox}$=1.48 during the high state. This low-state $\alpha_{\rm ox}$ almost makes it an X-ray-weak AGN according to the definition by

[4] The X-ray loudness is defined by Tananbaum et al. (1979) as $\alpha_{\rm ox} = -0.384 \log(f_{2\,\rm keV}/f_{2500\,\text{Å}})$.

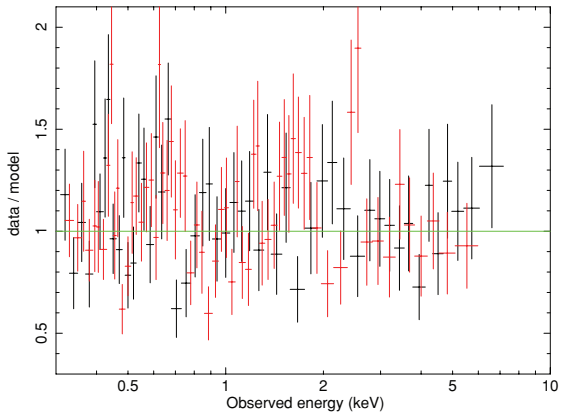

Figure 10. Ratio plot between the reflection model shown in Fig. 9 and the data with the low-state data shown in black and the high-state data in red.

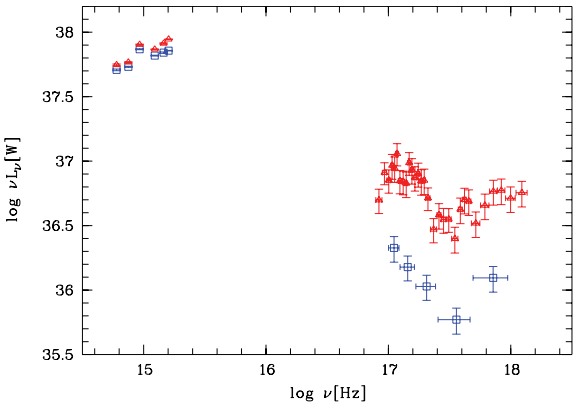

Figure 11. SEDs of PG 1211+143 during the low and high states on 2007 April 17 and 22 (segments 017 and 018, respectively). The low-state *Swift* UVOT and XRT data are displayed as (blue) squares and the high-state data as (red) triangles.

Brandt, Laor & Wills (2000), who define AGN with $\alpha_{ox} > 2.0$ as X-ray weak. The luminosities in the Big-Blue-Bump are $\log L_{BBB} = 38.42$ and 38.53 (W) for the low and high states, respectively. These luminosities correspond to Eddington ratios of $L/L_{Edd} = 0.26$ and 0.33, respectively, assuming a mass of the central black hole of $9 \times 10^7\,M_\odot$ (Vestergaard & Peterson 2006).

4 DISCUSSION

Based on the results from this study of the NLS1 PG 1211+143, we found that the short-time (and perhaps even the long-time) variations of the X-ray and optical/UV continuums do not seem to correlate well (Smith & Vaughan 2007, and the references within). While the X-ray continuum varied rapidly (more than five times during *Swift* monitoring campaign) with a general trend of brightness increase, the optical/UV continuum showed minimal changes with a general trend of brightness decrease. This is not unusual and is in fact reported for other objects (e.g. NGC 5548, Uttley et al. 2003). Such a behaviour sets constraints on different reprocessing scenarios. We are going to discuss briefly several possibilities, assuming that the optical/UV emission is produced by a standard, thin accretion disc, the central black hole mass is $M_{BH} \simeq 9 \times 10^7\,M_\odot$ and the accretion rate (in Eddington units) is $\dot{m} \simeq 0.3$ (Section 3.7). The accretion rate is also consistent within the errors with the one found by Kaspi et al. (2000) and Loska, Czerny & Szczerba (2004).

4.1 Cause of the X-ray weakness

As shown in Fig. 1, over the last 20 years PG 1211+143 appears to be fainter in X-rays compared with the X-ray observation during the 1980s. Especially during our *Swift* observations during the beginning of our monitoring in 2007 March, PG 1211+143 was found to be in an historical X-ray low state especially in the 0.2–2.0 keV band. The X-ray spectrum during the low state is somewhat similar to that found during the historical low state in Mkn 335 (Grupe et al. 2007b, 2008a). Also, here the low state could be explained by a strong partial covering absorber. Later, monitoring with *Swift* suggests that the absorber has disappeared again and that Mkn 335 is back in a high-state (Grupe et al., in preparation). Similarly, the low state here was just a temporary event that lasted for a maximum of about a year. Partial covering absorbers, however, can last significantly longer. One example is the X-ray transient NLS1 WPVS 007 (Grupe et al. 1995), which has developed strong broad absorption line features in the UV (Leighly et al. 2009) and a strong partial covering absorber in X-rays (Grupe, Leighly & Komossa 2008b). It has been in an extreme low X-ray state for more than a decade (Grupe et al. 2007a, 2008b).

Statistically, we cannot distinguish between the partial covering absorber or the reflection models. Both models result in similar χ^2/ν. Both models can also be fit self-consistently leaving the intrinsic X-ray spectrum fixed and only affected by either partial covering absorption or reflection.

In the case of a partial covering absorber, we can expect that the observed light is polarized like it has been seen in the NLS1 Mkn 1239 which is highly optically polarized and shows a strong partial covering absorber in X-rays (Grupe et al. 2004). However, both PG 1211+143 and Mkn 335 do not show any sign of optical continuum polarization (Berriman et al. 1999; Smith et al. 2002). Note, however, that all these polarimetry measurements were done when the objects were in their high state. There are no polarimetry measurements (at least not to our knowledge) that were performed during their low states. Therefore, the non-polarization in the optical does not exclude the partial covering model.

4.2 Compact central X-ray source or extended medium?

It is commonly assumed that the most part of the AGN X-ray emission is produced close to the centre, within the inner few tens R_g. The X-rays in radio-quiet objects may come from the inner part of an accretion disc, perhaps operating there in a mode of a very hot, geometrically thick, low-efficient accretion flow (e.g. advection-dominated accretion flow) or from an active corona, sandwiching the disc. In either case, when studying the X-ray irradiation of the *optically* emitting outer parts of the disc (at $\sim$100–1000R_g), the X-ray producing region could be considered as a point source, elevated slightly above the centre of the disc and illuminating the periphery. Thus, a part of this highly variable by presumption X-ray emission could be reprocessed into optical/UV emission, which variations will lag behind the X-ray variations.

The temperature of a thin (Shakura–Sunyaev) accretion disc scales with the radial distance r (in Schwarzschild radii) as $T(r) \simeq 610^5 (\dot{m}/M_8)^{1/4} r^{-3/4}$ (K) (Frank, King & Raine 2002). If a point-like X-ray source, located at some distance H above the disc close to the centre, irradiates the outer parts, it causes a temperature increase by a certain factor, but the radial temperature dependence happens to be the same (at least for $r \gg H$). Since most of the visual/UV light is presumably due to viscous heating, not due to irradiation, the temperature increase could be considered as a small addition to the usual

disc temperature. Nevertheless, the X-ray variations should transform into *some* optical/UV variations with a time delay, due to the light crossing time. If each disc ring emits mostly wavelengths close to the maximum of the *Planck* curve for the corresponding temperature, one expects the time delays to scale with the wavelength as $\tau_\lambda \simeq 5(\dot{m}M_8^2)^{1/3}\lambda_{5000}^{4/3}$ (d), which transforms to $\tau_\lambda \simeq 5\ \lambda_{5000}^{4/3}$ (d) for the accretion parameters accepted above.

The delay obtained from the fit in Section 3.5, however, appears to be approximately two times longer than expected, yet consistent with the expected dependence of $\lambda^{4/3}$. Although different fits to the data are possible, due to the uncertainties, the general offset seems to indicate a time inconsistency. A possible explanation may be searched in the spatial location of the X-ray source. Even if the very centre produces most of the X-ray emission, the outer disc may not 'see' much of it. Instead, a large-scale backscattering matter may be located at significant height above the disc, thus increasing the light-crossing time two to three times (Loska et al. 2004; Czerny & Janiuk 2007, see also their fig. 6). In fact, the presence of such a backscattering matter, in a form of a high-velocity outflow or a warm absorber, is suggested by independent studies of this object (Pounds et al. 2003; Pounds & Page 2006). One is to note, however, that for a similar otherwise object Mkn 335, the delays were found to be consistent with a direct irradiation from a compact central source (Czerny & Janiuk 2007). On the other hand, two recent studies by Arévalo et al. (2008) and Breedt et al. (2009) found significant correlation between the X-ray and optical bands at essentially zero time lag (yet, not necessarily inconsistent with the direct reprocessing, considering the uncertainties) for MR 2251–178 and Mkn 79, respectively. Finally, for a broad-line radio galaxy (3C 120), an otherwise different type of object, but with similar to PG 1211+143 black hole mass and accretion rate, Marshall et al. (2009) found a ∼28 d delay of *R*-band behind the X-rays, being longer than expected and similar to our findings. Since the results from these and other studies have not shown a systematic interband behaviour, one approach to resolve the problem could be to study separately different types of objects, grouped by their intrinsic characteristics, like central masses, accretion rates, line widths, X-ray and radio properties, etc. (e.g. Bachev 2009), in order to reveal how the presence of disc reprocessing might be related to overall quasar appearance.

On the other hand, instead from around the central black hole, the variable X-ray emission could come from many active regions (flares) in the corona, covering the optically emitting parts of the disc (Czerny et al. 2004). Such active regions (or hot spots) can irradiate the disc locally, producing almost instantaneous optical/UV continuum changes. The later can be significant enough to be observable under some conditions. The observed wavelength-dependent time delay, however, seems to make this possibility unlikely.

4.3 Why is the optical/UV continuum poorly responding to the X-ray changes?

A few factors can contribute to the apparent lack of significant correlation between the optical/UV and X-ray continua. First, the possibility that the X-ray emission is highly anisotropic (Papadakis et al. 2000) or the disc geometry is far from flat (bumpy surface, Cackett, Horne & Winkler 2007 or warps, Bachev 1999), leading only to a minor optical response to the huge otherwise X-ray changes, cannot entirely be ruled out. Yet, the observed approximately two times longer lags than expected are difficult to explain in terms of such an assumption, since in the presence of a large-scale backscattering medium, needed to account for the extra light travel path, the unevenness of the surface should be of little significance.

Another possibility which might explain the large X-ray variations and the absence of optical/UV is the presence of absorbing matter along the line of sight. If located close enough to the centre, it can partially obscure the compact X-ray source from the observer, but not too much from the larger, optically emitting part of the accretion disc. In such a case, indeed, the large X-ray variations observed would hardly be transferred into the optical bands. Unfortunately, the X-ray spectral fitting cannot distinguish well enough between reflection and absorption models to be able to determine which one shapes the X-ray continuum most.

4.4 X-ray emission – leading or trailing?

Taking into account the position of the highest maximum of the *I*-band ICCF (Fig. 6), the *I*-band changes appear to lead the X-ray ones. One way to explain this result, if real at all, is invoking the synchrotron self Compton (SSC) mechanism to account for part of the produced X-rays. SSC assumes that some of the near-IR photons might have a synchrotron origin, and could later be scattered by the same relativistic electrons to produce the X-ray flares, lagging behind the infrared. However, the available data set, based merely on the LCs information, cannot justify undisputedly such an explanation. Furthermore, no strong jet or significant radio emission is present in this object (where SSC is typically assumed to play a significant role). So, if SSC is to account for the delay of the X-ray behind the *I*-band, this process has to take place in a the base of a possible failed jet (Czerny et al. 2008, and the references therein) or in the central parts of the disc, where the disc could operate as a very hot flow, and where hot electrons and perhaps strong magnetic fields could be present.

5 SUMMARY

In this paper, we presented the results of a continuum (X-ray to optical *I*-band) monitoring campaign of PG 1211+143, performed with *Swift* and ground-based observatories. The main results are summarized below.

(i) In spite of being in a very low X-ray state, the quasar PG 1211+143 showed significant X-ray variations (up to five times) on daily basis, with only minor optical/UV flux changes. This behaviour indicates that a rather small amount of the hard radiation is reprocessed into longer wavelengths. Since both, reflection and absorption models fit equally well the X-ray spectrum, we are unable to determine the exact cause of the X-ray weakness of PG 1211+143 during its 2007 minimum.

(ii) Interband cross-correlation functions suggest that a wavelength-dependent time delay between the X-ray and the optical/UV bands is present, indicating that at least a part of the X-rays is reprocessed into longer wavelengths.

(iii) Although the $\tau - \lambda$ dependence followed the general trend expected for a thin accretion disc (i.e. $\tau_\lambda \sim \lambda^{4/3}$), the delays are approximately two times longer, implying the possible existence of a large-scale backscattering matter above the disc (wind/warm absorber), rather than a central point-like X-ray source, directly irradiating the disc.

(iv) Even if the object is radio quiet, with no strong jet known, we found indications that the SSC mechanism may play some role in the X-ray production.

ACKNOWLEDGMENTS

We are grateful to Neil Gehrels for approving our Target of Opportunity request and the *Swift* team for performing the Target of Opportunity observations of PG 1211+143. We would also like to thank the anonymous referee for his/her helpful comments and suggestions which significantly improved this paper. This research has made use of the NASA/IPAC Extragalactic Data base (NED) which is operated by the Jet Propulsion Laboratory, Caltech, under contract with the National Aeronautics and Space Administration. *Swift* is supported at PSU by NASA contract NAS5-00136. This research was supported by NASA contract NNX07AH67G (DG).

REFERENCES

Abrassart A., Czerny B., 2000, A&A, 356, 475
Arévalo P., Uttley P., Kaspi S., Breedt E., Lira P., McHardy I. M., 2008, MNRAS, 389, 1479
Arnaud K. A., 1996, ASP Conf. Ser. Vol. 101, Astronomical Data Analysis Software and Systems V. Astron. Soc. Pac., San Francisco, p. 17
Alexander T., 1997, in Maoz D., Sternberg A., Leibowitz E. M., eds, Astronomical Time Series. Dordrecht, Kluwer, p. 163
Bachev R., 1999, A&A, 348, 71
Bachev R., 2009, A&A, 493, 907
Bachev R., Marziani P., Sulentic J. W., Zamanov R., Calvani M., Dultzin-Hacyan D., 2004, ApJ, 617, 171
Berriman G., Schmidt G. D., West S. C., Stockman H. S., 1999, ApJS, 74, 869
Boller T., Brandt W. N., Fink H. H., 1996, A&A, 305, 53
Boroson T. A., 2002, ApJ, 565, 78
Brandt W. N., Mathus S., Elvis M., 1997, MNRAS, 285, L25
Brandt W. N., Laor A., Wills B. J., 2000, ApJ, 528, 637
Breedt E. et al., 2009, MNRAS, 394, 427
Burrows D. et al., 2005, Space Sci. Rev., 120, 165
Cackett E. M., Horne K., Winkler H., 2007, MNRAS, 380, 669
Chevalier C., Ilovaisky S. A., 1991, A&AS, 90, 225
Chevalier L., Collin S., Dumont A. M., Czerny B., Mouchet M., Goncalves A. C., Goosmann R., 2006, A&A, 449, 493
Czerny B., Janiuk A., 2007, A&A, 464, 167
Czerny B., Rozanska A., Dovciak M., Karas V., Dumont A.-M., 2004, A&A, 420, 1
Czerny B., Siemiginowska A., Janiuk A., Gupta A. C., 2008, MNRAS, 386, 1557
Done C., Nayakshin S., 2007, MNRAS, 377, L59
Edelson R. A., Krolik J. H., 1988, ApJ, 333, 646
Elvis M., 2000, ApJ, 545, 63
Elvis M., Wilkes B. J., Tananbaum H., 1985, ApJ, 292, 357
Fabian A. C., Rees M. J., Stella L., White N. E., 1989, MNRAS, 238, 729
Fabian A. C., Miniutti G., Gallo L. C., Boller Th., Tanaka Y., Vaughan S., Ross R. R., 2004, MNRAS, 353, 1071
Ferrarese L., Merritt D., 2000, ApJ, 539, 9
Frank J., King A., Raine D., 2002, Accretion Power in Astrophysics. Cambridge Univ. Press, Cambridge
Gallo L. C., 2006, MNRAS, 368, 479
Gallo L. C., Brandt W. N., Constantini E., Fabian A. C., 2007a, MNRAS, 377, 1375
Gallo L. C., Brandt W. N., Constantini E., Fabian A. C., Iwasawa K., Papadakas I. E., 2007b, MNRAS, 377, 391
Gaskell C. M., Peterson B. M., 1987, ApJS, 65, 1
Gaskell C. M., Sparke L. S., 1986, ApJ, 305, 175
Gehrels N. et al., 2004, ApJ, 611, 1005
Grupe D., 2004, AJ, 127, 1799
Grupe D., Beuermann K., Mannheim K., Thomas H.-C., Fink H. H., de Martino D., 1995, A&A, 300, L21
Grupe D., Thomas H.-C., Beuermann K., 2001, A&A, 367, 470
Grupe D., Mathur S., Komossa S., 2004, AJ, 127, 3161
Grupe D., Schady P., Leighly K. M., Komossa S., O'Brien P. T., Nousek J. A., 2007a, AJ, 133, 1988
Grupe D., Komossa S., Gallo L. C., 2007b, ApJ, 668, L111
Grupe D., Komossa S., Gallo L. C., Fabian A. C., Larsson J., Pradhan A. K., Xu D., Miniutti G., 2008a, ApJ, 681, 982
Grupe D., Leighly K. M., Komossa S., 2008b, AJ, 136, 2343
Janiuk A., Czerny B., Madejski G. M., 2001, ApJ, 557, 408
Hill J. E. et al., 2004, Proc. SPIE, 5165, 217
Kalberla P. M. W., Burton W. B., Hartmann D., Arnal E. M., Bajaja E., Morras R., Poppel W. G. L., 2005, A&A, 440, 775
Kaspi S., Smith P. S., Netzer H., Maoz D., Jannuzi B. T., Giveon U., 2000, ApJ, 533, 631
Kaspi S., Behar E., 2006, ApJ, 636, 674
Krolik J. H., 1999, Active Galactic Nuclei: from the Central Black Hole to the Galactic Environment. Princeton Univ. Press, Princeton, NJ
Landolt A. U., 1992, AJ, 104, 340
Larsson J., Miniutti G., Fabian A. C., Miller J. M., Reynolds C. S., Ponti G., 2008, MNRAS, 384, 1316
Leighly K. M., Mushotzki R. F., Nandra K., Foster K., 1997, ApJ, 486, L25
Leighly K. M., 1999a, ApJS, 125, 297
Leighly K. M., 1999b, ApJS, 125, 317
Leighly K. M., Hamann F., Casebeer D. A., Grupe D., 2009, ApJ, in press (arXiv:0906.2149)
Loska Z., Czerny B., Szczerba R., 2004, MNRAS, 355, 1080
Magorrian J. et al., 1998, AJ, 115, 2285
Marshall K., Ryle W. T., Miller H. R., Marscher A. P., Jorstad S. G., Chicka B., McHardy I. M., 2009, ApJ, 696, 601
Miniutti G., Fabian A. C., 2004, MNRAS, 349, 1435
Osterbrock D. E., Pogge R. W., 1985, ApJ, 297, 1660
Papadakis I. E., Brinkmann W., Negoro H., Detsis E., Papamastorakis I., Gliozzi M., 2000, preprint (astro-ph/0012317)
Poole T. et al., 2008, MNRAS, 383, 627
Pounds K. A., Page K. L., 2006, MNRAS, 372, 1275
Pounds K. A., Reeves J. N., 2007, MNRAS, 374, 823
Pounds K. A., Reeves J. N., King A. R., Page K. L., O'Brien P. T., Turner M. J. L., 2003, MNRAS, 345, 705
Roming P. W. A. et al., 2005, Space Sci. Rev., 120, 95
Roming P. W. A. et al., 2009, ApJ, 690, 163
Ross R. R., Fabian A. C., 2005, MNRAS, 358, 211
Schlegel D. J., Finkbeiner D. P., Davis M., 1998, ApJ, 500, 525
Smith R., Vaughan S., 2007, MNRAS, 375, 1479
Smith J. E., Young S., Robinson A., Corbett E. A., Giannuzzo M. E., Axon D. J., Hough J. H., 2002, MNRAS, 773, 798
Sulentic J. W., Zwitter T., Marziani P., Dultzin-Hacyan D., 2000, ApJ, 536, L5
Tananbaum H. et al., 1979, ApJ, 234, L9
Turner T. J., Miller L., 2009, A&AR, 17, 47
Turner T. J., Miller L., George I. M., Reeves J. N., 2006, A&A, 445, 59
Uttley P., Edelson R., McHardy I. M., Peterson B. M., Markowitz A., 2003, ApJ, 584, 53
Vestergaard M., Peterson B. M., 2006, ApJ, 641, 689

APPENDIX A: LOG OF OBSERVATIONS

Table A1. Summary of the *Swift* observations of PG 1211+143. Start and end times $T_{\rm start}$ and $T_{\rm end}$ of the observations are given in UT and all exposure times are given in units of s.

Segment	$T_{\rm start}$	$T_{\rm end}$	JD 2454000	$T_{\rm XRT}$	T_V	T_B	T_U	T_{W1}	T_{M2}	T_{W2}
001	2007 March 08 00:48	2007 March 08 02:35	167	1111	–	–	–	–	–	–
002	2007 March 09 01:03	2007 March 09 02:54	168	1781	148	148	148	298	373	596
003	2007 March 10 17:20	2007 March 10 22:17	169	1695	154	154	154	309	203	621
004	2007 March 11 19:03	2007 March 11 23:59	170	1711	154	154	154	310	217	621
005	2007 March 12 15:55	2007 March 12 20:52	171	1666	149	149	149	300	219	601
006	2007 March 13 20:50	2007 March 13 22:34	172	844	74	74	74	149	117	301
007	2007 March 14 09:10	2007 March 14 12:34	173	1995	168	168	168	336	403	670
008	2007 March 15 11:07	2007 March 15 13:02	174	1769	145	145	145	292	399	583
009	2007 March 16 00:02	2007 March 16 17:54	175	1566	142	145	145	295	82	593
010	2007 March 17 08:21	2007 March 17 19:12	176	2689	208	231	231	467	478	932
011	2007 March 18 10:05	2007 March 18 16:39	177	1738	149	149	149	300	292	601
012	2007 March 19 10:11	2007 March 19 16:45	178	1683	144	144	144	292	282	582
013	2007 March 26 07:09	2007 March 26 08:28	185	2006	166	166	166	331	444	664
014	2007 April 02 20:57	2007 April 02 22:36	192	2450	201	201	201	403	559	808
016	2007 April 11 09:12	2007 April 11 14:09	201	1756	157	157	157	318	233	633
017	2007 April 17 00:13	2007 April 17 06:46	207	2043	168	168	168	338	417	678
018	2007 April 22 11:53	2007 April 22 15:18	212	2063	171	171	171	342	434	684
019	2007 April 30 04:44	2007 April 30 06:32	220	1356	114	114	114	226	289	454
021	2007 May 09 15:13	2007 May 09 17:04	229	1398	70	139	139	277	183	539
022	2007 May 14 04:04	2007 May 14 05:59	234	2257	185	186	186	372	518	744
023	2007 May 20 01:28	2007 May 20 03:12	240	857	–	176	176	354	–	120
024	2008 February 17 07:56	2008 February 17 07:59	513	188	–	–	–	–	–	–

Table A2. XRT Count rates and hardness ratios and UVOT magnitudes of PG 1211+143. The UVOT magnitudes were corrected for Galactic reddening ($E_{B-V} = 0.035$; Schlegel et al. 1998).

Segment	CR	HR	V	B	U	$UVW1$	$UVM2$	$UVW2$
001	0.050 ± 0.007	-0.19 ± 0.13	–	–	–	–	–	–
002	0.057 ± 0.006	$+0.02 \pm 0.11$	14.32 ± 0.02	14.59 ± 0.01	13.33 ± 0.01	13.31 ± 0.01	13.16 ± 0.01	13.18 ± 0.01
003	0.049 ± 0.006	-0.27 ± 0.12	14.28 ± 0.02	14.56 ± 0.01	13.31 ± 0.01	13.25 ± 0.01	13.17 ± 0.01	13.12 ± 0.01
004	0.085 ± 0.008	-0.14 ± 0.09	14.26 ± 0.02	14.58 ± 0.01	13.29 ± 0.01	13.24 ± 0.01	13.15 ± 0.01	13.12 ± 0.01
005	0.119 ± 0.009	-0.21 ± 0.08	14.26 ± 0.02	14.56 ± 0.01	13.31 ± 0.01	13.26 ± 0.01	13.08 ± 0.01	13.11 ± 0.01
006	0.059 ± 0.009	-0.17 ± 0.15	14.29 ± 0.02	14.52 ± 0.01	13.33 ± 0.01	13.27 ± 0.01	13.07 ± 0.03	13.11 ± 0.01
007	0.071 ± 0.006	-0.09 ± 0.08	14.26 ± 0.02	14.56 ± 0.01	13.28 ± 0.01	13.23 ± 0.01	13.10 ± 0.01	13.09 ± 0.01
008	0.060 ± 0.006	$+0.08 \pm 0.06$	14.26 ± 0.02	14.58 ± 0.01	13.37 ± 0.01	13.28 ± 0.01	13.17 ± 0.01	13.18 ± 0.01
009	0.071 ± 0.007	-0.16 ± 0.10	14.29 ± 0.02	14.56 ± 0.01	13.29 ± 0.01	13.25 ± 0.01	13.22 ± 0.04	13.09 ± 0.01
010	0.059 ± 0.005	-0.10 ± 0.09	14.27 ± 0.02	14.54 ± 0.01	13.31 ± 0.01	13.26 ± 0.01	13.12 ± 0.01	13.12 ± 0.01
011	0.072 ± 0.007	-0.15 ± 0.09	14.29 ± 0.02	14.60 ± 0.01	13.33 ± 0.01	13.28 ± 0.01	13.12 ± 0.01	13.15 ± 0.01
012	0.045 ± 0.006	-0.05 ± 0.12	14.29 ± 0.02	14.60 ± 0.01	13.38 ± 0.01	13.27 ± 0.01	13.14 ± 0.01	13.13 ± 0.01
013	0.139 ± 0.009	-0.14 ± 0.06	14.27 ± 0.02	14.55 ± 0.01	13.30 ± 0.01	13.20 ± 0.01	13.08 ± 0.01	13.09 ± 0.01
014	0.171 ± 0.008	-0.22 ± 0.05	14.27 ± 0.02	14.57 ± 0.01	13.30 ± 0.01	13.24 ± 0.01	13.10 ± 0.01	13.11 ± 0.01
016	0.037 ± 0.005	-0.18 ± 0.13	14.28 ± 0.02	14.58 ± 0.01	13.32 ± 0.01	13.29 ± 0.01	13.15 ± 0.01	13.15 ± 0.01
017	0.060 ± 0.006	-0.17 ± 0.09	14.36 ± 0.02	14.68 ± 0.01	13.43 ± 0.01	13.37 ± 0.01	13.28 ± 0.01	13.32 ± 0.01
018	0.332 ± 0.013	-0.21 ± 0.04	14.26 ± 0.02	14.57 ± 0.01	13.34 ± 0.01	13.24 ± 0.01	13.10 ± 0.01	13.10 ± 0.01
019	0.095 ± 0.009	-0.16 ± 0.09	14.33 ± 0.02	14.58 ± 0.01	13.30 ± 0.01	13.24 ± 0.01	13.11 ± 0.01	13.16 ± 0.01
021	0.293 ± 0.015	-0.11 ± 0.05	14.26 ± 0.02	14.58 ± 0.01	13.32 ± 0.01	13.26 ± 0.01	13.11 ± 0.02	13.13 ± 0.01
022	0.294 ± 0.012	-0.15 ± 0.04	14.27 ± 0.02	14.60 ± 0.01	13.39 ± 0.01	13.26 ± 0.01	13.17 ± 0.01	13.17 ± 0.01
023	0.095 ± 0.011	-0.18 ± 0.11	–	14.61 ± 0.01	13.35 ± 0.01	13.30 ± 0.01	–	13.18 ± 0.01
024	0.375 ± 0.045	-0.10 ± 0.12	–	–	–	–	–	–

Table A3. Ground-based observations. All magnitudes are corrected for Galactic reddening ($E_{B-V} = 0.035$; Schlegel et al. 1998).

JD 2454000	*U*	*B*	*V*	*R*	*I*	Instrument
116.52	–	14.79 ± 0.10	14.29 ± 0.03	13.96 ± 0.01	13.75 ± 0.02	AOB
153.52	–	–	14.22 ± 0.04	–	–	AOB
157.39	–	14.49 ± 0.04	14.24 ± 0.02	13.91 ± 0.02	13.72 ± 0.02	RSh
171.63	13.28 ± 0.07	14.50 ± 0.03	14.25 ± 0.02	13.91 ± 0.02	13.73 ± 0.03	RSh
172.42	13.33 ± 0.05	14.51 ± 0.02	14.27 ± 0.02	13.93 ± 0.02	13.74 ± 0.02	RSh
174.34	–	14.58 ± 0.07	14.28 ± 0.02	13.94 ± 0.01	13.73 ± 0.01	AOB
175.35	–	14.57 ± 0.07	14.28 ± 0.02	13.93 ± 0.01	13.74 ± 0.01	AOB
176.31	–	14.47 ± 0.10	14.28 ± 0.02	13.94 ± 0.01	13.75 ± 0.01	AOB
176.45	13.32 ± 0.03	14.49 ± 0.03	14.26 ± 0.02	13.93 ± 0.02	13.72 ± 0.02	RSh
177.32	–	–	14.28 ± 0.03	13.96 ± 0.02	13.73 ± 0.03	AOB
178.32	–	14.55 ± 0.10	14.28 ± 0.02	13.92 ± 0.02	13.74 ± 0.02	AOB
179.47	–	14.57 ± 0.10	14.26 ± 0.02	13.94 ± 0.02	13.74 ± 0.02	AOB
199.49	–	14.50 ± 0.01	14.25 ± 0.01	13.98 ± 0.01	13.78 ± 0.01	R2m
200.43	–	14.51 ± 0.01	14.23 ± 0.01	13.97 ± 0.01	13.76 ± 0.01	R2m
201.44	–	14.56 ± 0.03	14.22 ± 0.03	13.94 ± 0.03	–	R2m
201.45	–	14.57 ± 0.02	14.23 ± 0.01	13.97 ± 0.01	13.75 ± 0.01	RSh
203.32	–	14.57 ± 0.01	14.23 ± 0.03	14.00 ± 0.01	13.78 ± 0.01	RSh
204.34	–	14.63 ± 0.01	14.23 ± 0.01	13.97 ± 0.01	13.78 ± 0.01	RSh
208.49	13.39 ± 0.03	14.56 ± 0.02	14.28 ± 0.02	13.97 ± 0.02	13.77 ± 0.02	RSh
210.41	13.35 ± 0.02	14.56 ± 0.02	14.29 ± 0.02	13.97 ± 0.02	13.76 ± 0.02	RSh
211.38	13.39 ± 0.03	14.59 ± 0.02	14.31 ± 0.01	13.99 ± 0.02	13.77 ± 0.02	RSh
213.29	–	14.60 ± 0.05	14.31 ± 0.02	13.94 ± 0.01	13.76 ± 0.02	AOB
217.29	–	14.56 ± 0.05	14.36 ± 0.03	13.99 ± 0.02	13.77 ± 0.02	AOB
230.35	–	14.62 ± 0.05	14.28 ± 0.02	13.96 ± 0.01	13.76 ± 0.01	AOB
231.30	–	14.61 ± 0.05	14.27 ± 0.02	13.95 ± 0.01	13.74 ± 0.01	AOB
232.31	–	14.63 ± 0.06	14.29 ± 0.02	13.95 ± 0.02	13.74 ± 0.02	AOB
233.42	–	14.59 ± 0.05	14.38 ± 0.02	13.98 ± 0.01	13.78 ± 0.01	AOB
234.30	–	14.66 ± 0.06	14.23 ± 0.02	13.98 ± 0.01	13.77 ± 0.01	AOB
236.32	–	14.60 ± 0.07	14.31 ± 0.02	13.98 ± 0.01	13.77 ± 0.01	AOB
238.37	–	14.57 ± 0.01	14.23 ± 0.01	13.91 ± 0.01	–	R2m
247.45	–	14.56 ± 0.02	14.29 ± 0.03	13.99 ± 0.03	13.81 ± 0.03	RSh
260.39	13.35 ± 0.05	14.60 ± 0.03	14.31 ± 0.02	14.00 ± 0.02	13.82 ± 0.02	RSh
261.36	–	14.62 ± 0.15	14.38 ± 0.02	14.02 ± 0.02	13.83 ± 0.02	AOB
262.40	–	14.65 ± 0.03	–	14.01 ± 0.02	13.79 ± 0.03	RSh
263.36	–	14.61 ± 0.03	14.33 ± 0.02	13.97 ± 0.02	13.81 ± 0.03	RSh
265.35	–	14.64 ± 0.10	14.39 ± 0.02	14.05 ± 0.02	13.87 ± 0.02	AOB
265.42	–	14.68 ± 0.02	14.35 ± 0.02	14.00 ± 0.03	13.84 ± 0.02	RSh
266.40	–	14.66 ± 0.02	14.33 ± 0.02	14.01 ± 0.02	13.81 ± 0.02	RSh
289.31	–	14.72 ± 0.13	14.36 ± 0.02	14.01 ± 0.02	13.84 ± 0.02	AOB
290.35	–	14.76 ± 0.13	14.35 ± 0.02	14.01 ± 0.02	13.85 ± 0.03	AOB
291.34	–	14.69 ± 0.02	14.32 ± 0.02	14.06 ± 0.01	13.89 ± 0.01	RSh
292.31	–	14.68 ± 0.02	14.28 ± 0.02	14.03 ± 0.01	13.87 ± 0.01	RSh
292.36	–	–	14.32 ± 0.06	13.95 ± 0.06	–	AOB
293.32	–	14.67 ± 0.01	14.38 ± 0.02	14.04 ± 0.01	13.85 ± 0.01	RSh
296.33	–	14.73 ± 0.03	14.38 ± 0.02	14.02 ± 0.01	–	RSh
298.30	–	14.62 ± 0.03	14.37 ± 0.02	14.03 ± 0.03	13.85 ± 0.03	RSh
299.30	13.51 ± 0.09	14.66 ± 0.03	14.36 ± 0.02	14.02 ± 0.02	13.86 ± 0.03	RSh
303.30	–	14.81 ± 0.02	14.38 ± 0.01	14.07 ± 0.01	13.89 ± 0.02	R2m

This paper has been typeset from a TEX/LATEX file prepared by the author.

© 2009 The Authors. Journal compilation © 2009 RAS, MNRAS **399,** 750–761